PAPER • OPEN ACCESS

Efficient laser-driven proton and bremsstrahlung generation from cluster-assembled foam targets

New Journal of Physics
The open access journal at the forefront of physics

Deutsche Physikalische Gesellschaft DPG
IOP Institute of Physics

Published in partnership with: Deutsche Physikalische Gesellschaft and the Institute of Physics

OPEN ACCESS

RECEIVED
14 April 2021

REVISED
17 August 2021

ACCEPTED FOR PUBLICATION
20 August 2021

PUBLISHED
9 September 2021

PAPER

Efficient laser-driven proton and bremsstrahlung generation from cluster-assembled foam targets

Irene Prencipe[1,*], Josefine Metzkes-Ng[1], Andrea Pazzaglia[2], Constantin Bernert[1,3], David Dellasega[2], Luca Fedeli[2,4], Arianna Formenti[2], Marco Garten[1,3], Thomas Kluge[1], Stephan Kraft[1], Alejandro Laso Garcia[1], Alessandro Maffini[2], Lieselotte Obst-Huebl[1,3,5], Martin Rehwald[1,3], Manfred Sobiella[1], Karl Zeil[1], Ulrich Schramm[1,3], Thomas E. Cowan[1,3] and Matteo Passoni[2]

[1] Institute of Radiation Physics, Helmholtz-Zentrum Dresden-Rossendorf, Dresden, Germany
[2] Energy Department, Politecnico di Milano, Milan, Italy
[3] Technische Universität Dresden, Dresden, Germany
[4] LIDYL, CEA-Université Paris-Saclay, CEA Saclay, 91191 Gif-sur-Yvette, France
[*] Author to whom any correspondence should be addressed.
[5] Present address: Lawrence Berkeley National Laboratory, Berkeley, United States.

E-mail: i.prencipe@hzdr.de

Keywords: laser-driven ion acceleration, laser-driven bremsstrahlung generation, TNSA, near-critical density plasma, nanostructured targets, foam targets

Abstract

The interaction between intense 30 fs laser pulses and foam-coated 1.5 μm-thick Al foils in the relativistic regime (up to 5×10^{20} W cm^{-2}) is studied to optimize the laser energy conversion into laser-accelerated protons. A significant enhancement is observed for foam targets in terms of proton cut-off energy (18.5 MeV) and number of protons above 4.7 MeV (4×10^9 protons/shot) with respect to uncoated foils (9.5 MeV, 1×10^9 protons/shot), together with a sixfold increase in the bremsstrahlung yield. This enhancement is attributed to increased laser absorption and electron generation in the foam meso- and nanostructure.

1. Introduction

The hot, dense plasmas generated in the irradiation of solid targets with relativistic ($I > 10^{18}$ W cm^{-2} at $\lambda \sim 1$ μm) laser pulses provide a source for electrons [1], ions [2, 3] and x-rays [4, 5]. The efficiency of radiation generation is strongly determined by the laser energy conversion into hot electrons during the primary laser-target interaction, limited to the skin depth region of ~10 nm thickness in the case of flat solid-density targets. In the last decade, surface structures such as spatial modulations or lower-density layers have been investigated intensely to optimize laser absorption and secondary radiation generation [5–20]. Available enhancement strategies entail modifications of the laser light propagation (e.g. self-focusing) and/or an increase of the interaction volume or surface where plasma electrons can interact with the laser pulse. Modulated target surfaces with known roughness [7], laser induced periodic surface structures [8], gratings [9], arrays of nanospheres [10], nanowires [11] and pillars [12, 13] and conic targets [14, 15] have been proven to influence the laser absorption due to several effects, such as: increased specific surface area [8, 10–14], incidence under randomized angles [7], multiple reflections [7], tuning of the target dielectric function [8], resonant surface wave excitation [9], multi-pass stochastic heating [10], grazing incidence [11–15].

Of particular interest are near-critical targets enabling volume interaction mechanisms otherwise not allowed in solid density targets [16–22]. Their density is tuned to the *critical density* n_c, i.e. the transparency threshold for light propagation in a plasma, defined as $n_c = m_e\omega_L^2/4\pi e^2$, where m_e and e are the electron mass and charge and ω_L is the frequency of the incoming laser pulse. In the relativistic regime, the transparency threshold increases to $n_{\gamma c} = \gamma n_c$, where $\gamma = \sqrt{1 + a_0^2/2}$ is the electron average Lorentz factor

in the case of linearly polarized light and a_0 is the normalized laser amplitude, thus leading to the onset of relativistic transparency [23, 24]. It must however be noted that this model does not consider striction and relativistic nonlinearities, which would decrease the density threshold due to electron pile up at the laser rising edge, as shown in previous works [25, 26]. For Ti:sapphire lasers ($\lambda \cong 800$ nm), the non-relativistic critical density is about 1.7×10^{21} cm^{-3}, that corresponds to 5.8 mg cm^{-3} for fully ionized carbon plasma. Materials with density in this range include *foams* and normally present a structure that alternates voids and regions with density close to the solid density [27]. Therefore, the average density rather than the local density is to be considered near-critical.

In the case of a uniform and relativistically transparent foam, a partially cavitated channel forms in the plasma as electrons are expelled from the pulse propagation path due to the ponderomotive force [28, 29]. The radial dependence of the refractive index in the ponderomotive channel leads to self-focusing and steepening of the pulse rising edge [22]. Electrons are accelerated by direct laser acceleration (DLA) [30] and confined in the channel by the self-generated azimuthal magnetic field, while the electric field in the depleted region results in radial ion acceleration from the channel [31]. Foams composed of a uniform distribution of single wall carbon nanotubes have been shown to enhance the laser intensity due to pulse self-focusing and steepening and to generate superponderomotive electrons, resulting in enhanced ion acceleration when coupled with diamond-like carbon substrates [16–18]. Conversely, cluster-assembled foams characterized by a fractal structure and non-uniformities on the length scale of the laser wavelength can be reasonably expected to deviate from the uniform foam model, adding complexity to an already rich physical picture.

The interaction between high-intensity lasers and foams with structures on the sub-μm scale has been investigated by means of 3D particle-in-cell (PIC) simulations [32] in previous works [33–35]. These simulations can provide useful information on the interaction dynamics, even though they come with some limitations due to their considerable computational cost. Typically, to be able to carry out 3D PIC simulations of plasmas made of sub-micrometric solid-density clusters, compromises must be made in terms of resolution, plasma density and cluster size. As a result, the simulated structures are more uniform than real cluster-assembled foams (i.e. the simulated foams have an average density similar to that of real foams but a lower void fraction), potentially leading to discrepancies between the numerical model and experimental results. Nevertheless, 3D PIC simulations are useful to guide the physical understanding of laser-plasma interaction with such complex inhomogeneities. Previous numerical studies show that the peculiar foam structure allows laser propagation through the voids of the foam, resulting in different behaviours depending on the interaction regime, specifically on the transparency conditions (hence on the laser intensity and plasma average density). For instance, depending on the laser intensity, one can observe that foam plasmas may lead to strongly enhanced laser absorption, electron acceleration mechanisms different from those expected in homogeneous near-critical plasmas and isotropic ion acceleration from the Coulomb-like explosion of the aggregates composing the foam [33].

Experimentally, laser absorption enhancement from cluster-assembled foams deposited on μm-thick Al foils (*foam targets*) was demonstrated in studies focusing on proton acceleration via a mechanism termed target normal sheath acceleration (TNSA) [3, 19, 20, 36]. In this scheme, hot electrons produced in the interaction of the laser pulse with a μm-thick target propagate through the target and form an electron sheath at the rear surface, generating a quasi-static electric space-charge field that reaches ∼TV/m and is capable of accelerating protons to 10 s of MeV. The TNSA field strength scales with $E \sim \sqrt{n_e T_e}$, where n_e is the electron density and T_e the mean electron energy in the sheath field, making proton acceleration a sensitive indicator for absorption efficiency. A promising increase of the proton cut-off energy, E_{p+}, by a factor of 1.4, and number, N_{p+}, by a factor 1.7 for protons above 8 MeV, was observed for 8 μm foams with respect to Al reference targets irradiated with p-polarized light in the 10^{19}–10^{20} W cm^{-2} intensity range [19, 20]. Furthermore, proton acceleration was shown to be independent of polarization for foam targets. A significant enhancement was also observed for sub-relativistic laser intensity (10^{16}–10^{17} W cm^{-2}), with foam targets enabling acceleration of protons in the MeV range, corresponding to a 2–3 fold enhancement of the maximum proton energy with respect to uncoated Al foils [36]. These findings show that proton acceleration results depend on both laser features and foam parameters, in agreement with numerical results in [28].

Despite the previous experimental and theoretical efforts, important details of the laser-foam interaction in terms of light propagation in the structured foam and absorption dynamics have not been addressed experimentally so far, also because of the high laser temporal intensity contrast required not to disrupt the foam structure before the arrival of the main pulse. Moreover, data other than the proton acceleration efficiency should be considered in order to obtain more complete information on the physics of the interaction.

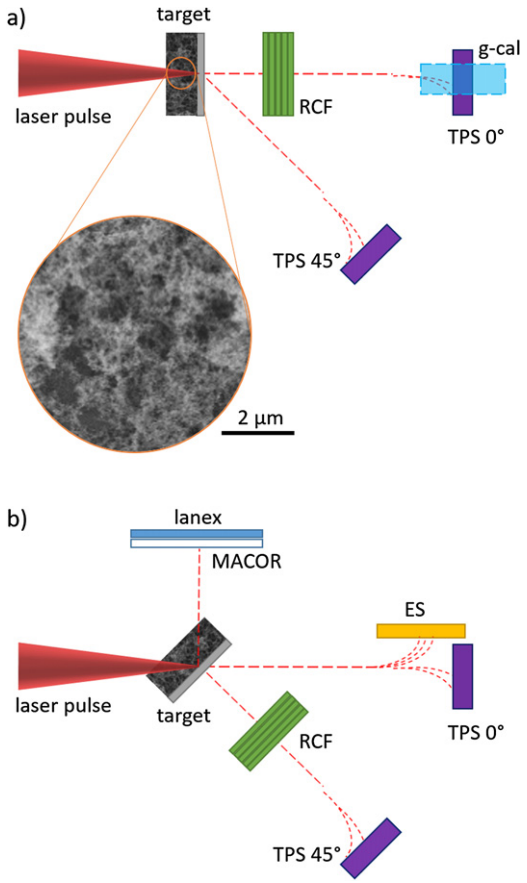

Figure 1. Schematic illustration of the experimental setup (top view) for normal (a) and 45° (b) incidence. Accelerated protons were characterized with stacks of radiochromic films (RCFs) and Thomson parabola spectrometers (TPSs). For normal incidence, Bremsstrahlung spectra were measured using a gamma calorimeter (g-cal). For 45° incidence, electron spectra were measured using a magnetic electron spectrometer (ES); patterns of reflected light (800 nm) and second harmonics (400 nm) were detected imaging a scatter screen (MACOR) to a CCD; the spatial distribution of electrons in the laser specular direction was characterized imaging a Lanex to a CCD. Inset: scanning electron micrograph showing the foam morphology.

Here we present an experimental investigation of the interaction of relativistic laser pulses with cluster-assembled foam targets and consequent secondary radiation generation (electrons, bremsstrahlung photons and ions). An extended set of diagnostics recording signatures of the light propagation and electron dynamics in the target shed light on the laser-foam interaction mechanisms. We show that the enhanced laser absorption results in an increase in the number of electrons contributing to the TNSA field. Electrons are accelerated into a large solid angle in the foam, explaining the dependence of experimental results on the foam thickness. Proton acceleration enhancement factors higher than those observed in previous experiments [19, 20, 36] have been measured in this experiment thanks to improved foam properties and optimised experimental settings.

2. Experimental configuration

The experiment was performed at the Draco 150 TW laser facility of Helmholtz-Zentrum Dresden-Rossendorf (Germany), a Ti:sapphire laser system delivering 30 fs, 0.5–2 J, *p*-polarized pulses with 800 nm centre wavelength on target after plasma mirror cleaning, resulting in a temporal intensity contrast of about 10^{-13} at 100 ps (10^{-10} at 5 ps) [37–39]. Plasma mirror cleaning is crucial to avoid early plasma expansion and preserve the foam structure until the interaction with the pulse peak. The experimental setup is schematically shown in figure 1. An intensity up to 5×10^{20} W cm^{-2} was obtained in a 2.8 μm FWHM focal spot with an f/2.5 off-axis parabolic mirror. Samples were irradiated under both normal (figure 1(a)) and 45° incidence (figure 1(b)).

Foam targets composed of a 1.5 μm thick Al foil and a 4–16 μm thick, slightly overcritical foam layer (18 ± 2 mg cm^{-3}, corresponding to $3.2n_c$) were produced and characterized in the Micro and Nanostructured Materials Laboratory at Politecnico di Milano (Italy) [20, 40–42]. Foams were directly deposited onto Al foils by pulsed laser deposition. This technique is based on the ablation of a graphite

target by means of a 532 nm nanosecond pulsed laser in Ar atmosphere, resulting in the production of carbon nanoparticles of about 10–20 nm diameter. The fractal structure of the material is determined by the in-flight aggregation dynamics of the nanoparticles during deposition, leading to the formation of micron-sized porous and void-rich mesoaggregates [43]. Deposited foams show non-uniformities on a scale comparable to the laser wavelength. For the deposition parameters described in previous works [20, 40], this resulted in incomplete substrate coverage for foams thinner than 8 μm. Therefore the foam deposition process onto 1.5 μm thick Al foils had to be optimized for this experiment to produce thinner foams down to 4 μm without degrading the substrate coverage (inset in figure 1(a)). In particular, 4 μm thick foams were produced using 200 mJ laser pulses and 1000 Pa pressure of argon as buffer gas. The deposition technique has the technological advantage that foams of different compositions, for example carbon, copper or tungsten, can be deposited in thin layers onto any kind of substrate [44]. Uncoated 1.5 μm thick Al foils irradiated in the same configuration as the foam targets were used as reference targets.

Accelerated ions were detected with multi channel plate Thomson parabola spectrometers (TPSs) in the laser propagation direction (TPS-0°) and under 45° (TPS-45°), detecting protons down to 3.3 MeV and 1.0 MeV, respectively. For selected shots, stacks of radiochromic films (RCFs) were mounted parallel to the target surface at a distance of 5.5 cm for proton beam profile and proton number characterization. RCF stacks used in this experiment are sensitive to proton energies down to 4.7 MeV. While most RCF stacks were perforated to allow simultaneous TPS measurements (the hole covering a solid angle of about 40 mrad), a few were left intact for calibrated proton spectrum reconstruction (for normal incidence only). Emitted bremsstrahlung radiation was measured for normal incidence using an image plate (IP) based calorimeter (g-cal) [45]. This is a sampling calorimeter composed by a sequence of layers of different materials (7×7 cm^2) and increasing thicknesses (for a total length of 12.4 cm) acting as absorbers and enabling the development of a secondary particle shower and IPs as active layers, similar to that described in [46]. The g-cal was positioned outside of the vacuum chamber over the TPS-0°, looking at the target from 17° above the horizontal plane and covering a solid angle of about 0.13 msr. The gamma calorimeter is sensitive to photon energies up to about 3.5 MeV. Furthermore, the following diagnostics were available for 45° incidence on target. A ceramic scatter screen (MACOR) was positioned along the laser specular reflection direction and imaged through band-pass filters to detect reflected light (800 nm) and second harmonics emission (400 nm) enabling characterization of the laser pulse propagation in the foam. The field of view of this diagnostic covers the full solid angle of the specularly reflected laser beam (120 msr). Electron acceleration from the target front surface in the specular direction was recorded by imaging a thin scintillator screen (Lanex) positioned behind the scatter screen [47, 48]. Scatter screen and Lanex were only available for 45° incidence on target. Escaping electrons were detected for 45° incidence by a magnetic electron spectrometer (ES) combined with the TPS-0°.

3. Results

3.1. Proton acceleration

Figures 2 and 3 give an overview of the proton acceleration results. Data indicate the strongest enhancement of the proton acceleration process for 4 μm thick foam irradiated at maximum laser intensity under normal incidence with respect to Al reference targets. In this condition, maximum proton energy, E_{p+}, of 18.5 ± 1.0 MeV was observed for 4 μm foam targets to be compared with 9.5 ± 0.9 MeV measured for Al. A fourfold increase in the number of accelerated protons per shot was measured integrating the proton signal in RCF stacks sensitive to protons with energy down to 4.7 MeV. 4×10^9 and 1×10^9 protons were detected for 4 μm foam and reference targets, respectively.

Figures 2(a) and (b) show a strong dependence of acceleration performance on the foam thickness, irradiation angle and laser energy, with a monotonic decrease of proton maximum energy and number for increasing foam thickness. Proton energy and number are normalized to the values measured for Al targets in the same irradiation conditions (i.e. same incidence angle and laser energy on target). These quantities are plotted against the foam effective thickness, $d_{\mathrm{eff}} = d/\cos(\alpha)$, where d is the foam nominal thickness and α is the incidence angle, to account for the longer laser and electron propagation path in the foam for 45° incidence. Proton numbers calculated from RCF stacks are only shown for normal incidence.

Moderate or no enhancement was observed for thicker foams and 45° incidence. $E_{p+}(12\ \mu\mathrm{m}, 0°)/E_{p+}\ (\mathrm{Al}, 0°) \cong 1.4$ and $E_{p+}(4\ \mu\mathrm{m}, 45°)/E_{p+}\ (\mathrm{Al}, 45°) \cong 1.3$ are considerably lower than the factor 2 measured for 4 μm at normal incidence. The proton cut-off energy measured for Al irradiated under 45° incidence, 10.3 ± 1.4 MeV, is comparable to that measured for Al under normal incidence (9.5 ± 0.9 MeV). Similar trends are also observed for lower laser intensities for normal incidence (0.5–2 J corresponding to intensities ranging from 1.3×10^{20} W cm^{-2} to 5×10^{20} W cm^{-2}), even though

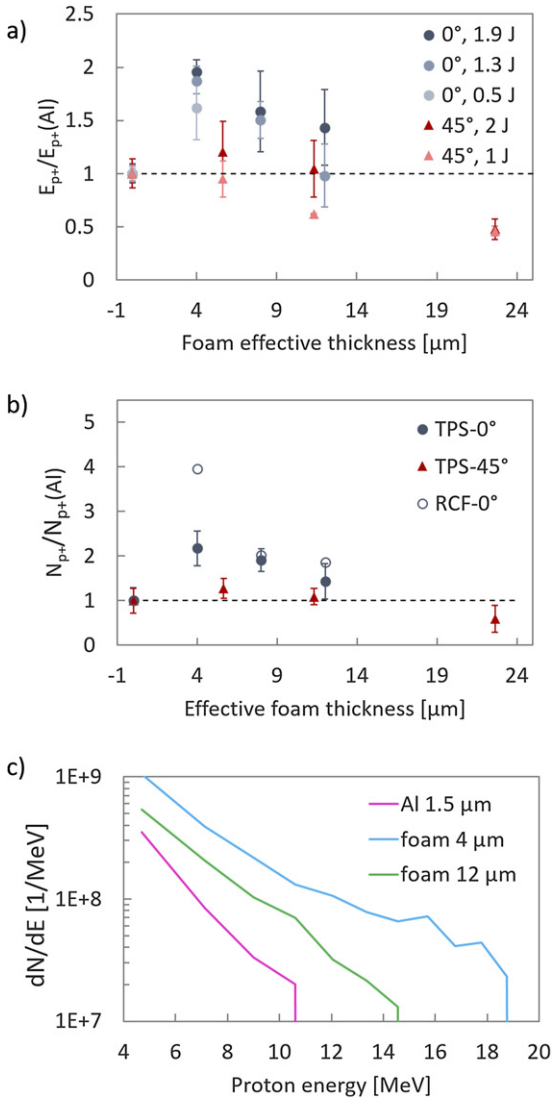

Figure 2. (a) Proton cut-off energy measured for 0° and 45° incidence in target normal direction (i.e. with TPS-0° and TPS-45°, respectively), normalized to the maximum energy measured for Al in each experimental configuration, plotted as a function of the foam effective thickness for laser energies between 0.5 J and 2 J (corresponding to 1.3×10^{20} W cm^{-2}–5×10^{20} W cm^{-2}). Data points represent the average $\boldsymbol{E_{p+}}$ calculated for about 6 shots for maximum laser intensity and 2 to 3 shots for lower intensities. The error bars represent the corresponding standard deviation. (b) Number of accelerated protons measured at maximum laser intensity with TPS-0° and TPS-45° (integrated respectively between 3.3 MeV and 1.0 MeV) and $\boldsymbol{E_{p+}}$, and for normal incidence only with RCF stacks (integrated between 4.7 MeV and $\boldsymbol{E_{p+}}$). Proton numbers are normalized to values obtained for 1.5 μm thick Al for each experimental condition and plotted versus the foam effective thickness. (c) Single-shot proton spectra reconstructed from dose deposition in RCF stacks for maximum laser intensity and normal incidence.

the maximum gain tends to decrease for lower intensities. No enhancement is observed at lower intensity (1.8×10^{20} W cm^{-2}) for 45° incidence.

The thickness dependence is also reflected in single-shot proton spectra reconstructed from dose deposition in RCF stacks for maximum laser intensity and normal incidence (figure 2(c)). Although spectra cannot be fitted with a single exponential to retrieve a proton temperature, the gentler slope observed for protons accelerated using foam targets is indicative of increased proton average energy with respect to Al targets.

Representative proton beam profiles recorded by RCF are shown in figure 3(a) for normal incidence and maximum laser intensity. While the typical profiles for Al foils are always characterized by filaments and spatial non-uniformities, smooth profiles can be observed for foam coated targets. The presence of structures in proton beam profiles from flat targets have been intensively investigated for both insulator and metal targets [49–52]. This has been attributed to spatial modulations of the electron sheath at the target rear arising from surface instabilities (for example Rayleigh–Taylor or Weibel instabilities) or from filamentation during electron propagation in the target bulk. Previous work on proton acceleration from targets composed of nanostructures on a flat foil showed that electrons accelerated from the multifaceted

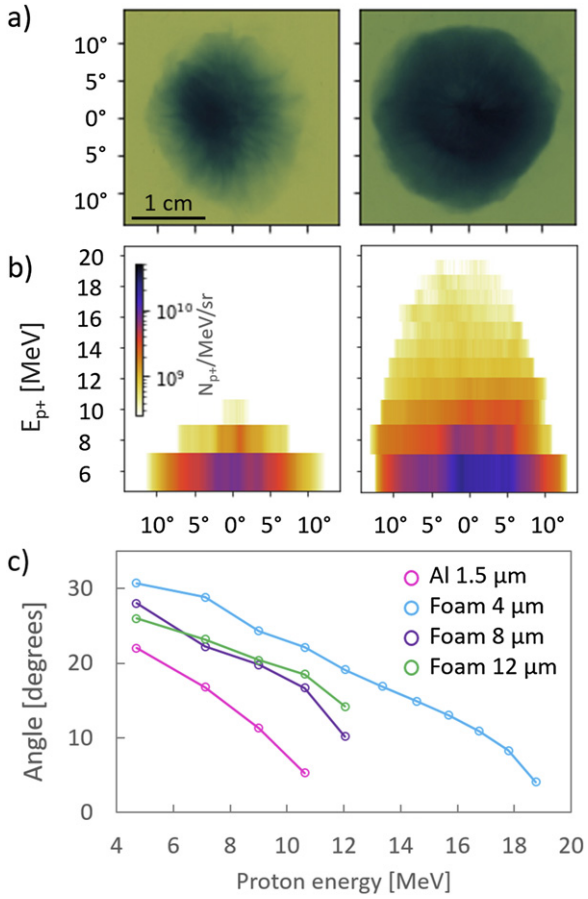

Figure 3. Spatial distributions of proton pulses obtained from RCF stacks for normal incidence and maximum laser intensity. (a) Proton beam profiles for Al (left) and 4 μm foam (right). Proton beam profiles were measured with the first film in the RCF stack, sensitive to protons with energy above 4.7 MeV. (b) Proton horizontal emission distribution from RCF stacks, displayed for Al (left) and 4 μm foam (right). (c) Energy dependent divergence of the proton beam calculated from representative RCF stacks.

surface of the nanostructured target can be expected to have a broad angular distribution and to mitigate spatial modulations of the electron sheath and, consequently, of the proton beam profile [53].

Figures 3(b) and (c) show the proton horizontal emission distribution (for Al and foam 4 μm only) and the energy dependent divergence of the proton beam, both calculated from representative RCF stacks for normal incidence and maximum laser intensity. These graphs show that proton beam profiles tend to be larger for foam targets, i.e. protons have a wider angular distribution.

For foam targets, in addition to proton emission in target normal direction, protons with energies up to 3 MeV (normal incidence) and 4 MeV (45° incidence) were detected 45° from target normal, i.e. by TPS-45° and TPS-0° respectively. This signal is significantly weaker than that observed for protons in target normal. No signal was observed for reference Al targets. This can be interpreted as evidence of non-directional proton emission from the foam. In fact, even though protons with energy of 3–4 MeV are not visible in RCF stacks, the proton emission cone observed in RCF stacks for 4.7 MeV TNSA protons extends to maximum 15° from target normal for foam targets. Therefore, it would be unreasonable to assume a 45° (or greater) emission cone for 4 MeV TNSA protons. According to previous studies, non-directional proton emission can be attributed to Coulomb explosion of the nanoparticles that are the building blocks of the foam [54].

3.2. Carbon ionization states

Enhanced acceleration performances were also observed for C^{6+} ions under normal incidence: maximum energies of 100 ± 15 MeV, 63 ± 30 MeV and 62 ± 25 MeV (uncertainties are given by the standard deviation) were measured at maximum laser intensity for 4 μm, 8 μm and 12 μm foam, respectively, to be compared to a cut-off energy of 37 ± 3 MeV measured for reference targets. For normal incidence, TPS data show a clear increase in C^{6+} yields for foam targets, with a trend similar to that observed for proton yields. A modest enhancement in the cut-off energy of C^{6+} was observed for 45° incidence with maximum laser energy: 47 ± 17 MeV and 41 ± 20 MeV for 4 μm and 8 μm foam targets, to be compared to 39 ±

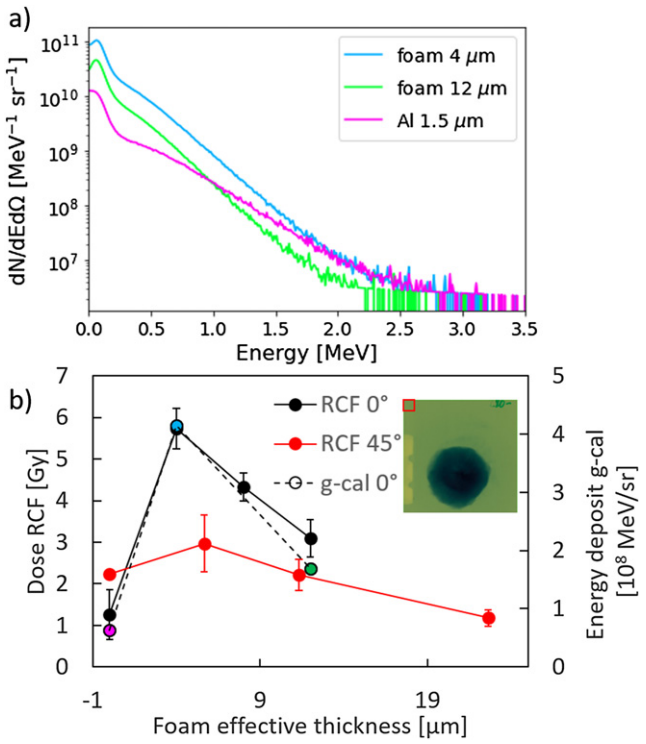

Figure 4. (a) Bremsstrahlung spectra measured for normal incidence for 4 μm and 12 μm foams and for Al reference target. Spectra are integrated over three shots due to the calorimeter sensitivity and normalised to obtain an average spectrum per shot. b) Bremsstrahlung yield detected by RCF (dose, primary y-axis) and g-cal (energy deposit in IPs, secondary y-axis). Single-shot yields are measured from an area in the first RCF film of each stack about 30° from target normal (region highlighted in the inset) and averaged over 2–3 shots. Error bars represent the corresponding standard deviation. Bremsstrahlung yields measured with g-cal are intrinsically averaged over three shots. Colours of g-cal data points indicate different thicknesses of foam layers and correspond to the legend of figure 5(a).

1 MeV measured for Al targets. However, a drop in C^{6+} yields was measured for foams irradiated under 45° incidence with respect to Al target, with lower ionization states becoming dominant especially for thicker foams, to the point that no C^{6+} trace is visible for 16 μm foam.

3.3. Bremsstrahlung generation

Figure 4(a) shows Bremsstrahlung spectra detected for normal incidence by the g-cal and unfolded via a Bayesian algorithm [55]. Bremsstrahlung spectra recorded for 4 and 12 μm foam show the same slope, with increased bremsstrahlung generation in the low energy range (up to 1.5 MeV) compared to Al. The main limitation of this diagnostic is that the calorimeter was positioned outside the vacuum chamber, in the target line of sight behind a glass window. This resulted in signal attenuation, especially for the lower energy spectral components, and consequent spectra hardening. In addition, the g-cal is in principle sensitive to bremsstrahlung generated by escaping electrons interacting with the chamber walls. However, this would produce shapes or gradients in the IPs because the g-cal is positioned above the TPS 0°, significantly higher than the incidence plane, and does not have a direct line of sight to the area where the highest number of electrons are expected to hit the chamber walls, due to the presence of optomechanics and other setup components. These components would shadow the signal coming from the chamber walls. Moreover, a vertical gradient would have been observed in the IPs if the signal had come mainly from the intersection between the chamber wall and the plane of incidence. Such effects however were not observed in our data. Therefore, Bremsstrahlung generated at the chamber walls is not expected to contribute significantly to the energy deposit in the calorimeter.

Bremsstrahlung yields were quantified as a function of foam thickness by integrating the bremsstrahlung spectra (figure 4(b)). In agreement with trends observed for proton energy and number for normal incidence, a maximum enhancement factor of 6.5 in the Bremsstrahlung yield was measured for 4 μm foam with respect to the reference Al target, indicating a higher number of electrons contributing to the bremsstrahlung generation for 4 μm foam. The bremsstrahlung yield quickly decreases for thicker foams. This observation is corroborated by bremsstrahlung radiation yields measured from RCF stacks. The bremsstrahlung dose was calculated in an area of 50 $\times$ 50 pixels^2 (about 4.3 $\times$ 4.3 mm) in the outer region of the RCF, about 30° from target normal, as shown in the inset in figure 4(b). RCF stacks and g-cal

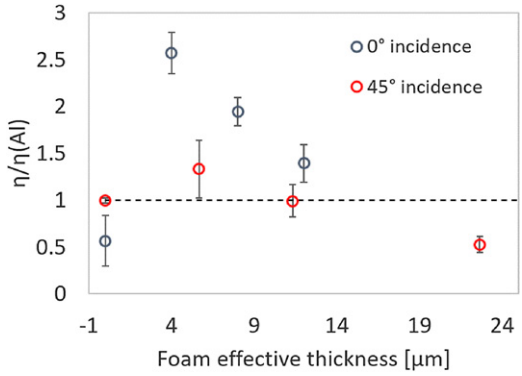

Figure 5. Relative conversion efficiency of laser energy into Bremsstrahlung energy normalised to the conversion efficiency measured for reference targets irradiated under 45° with maximum laser intensity. Conversion efficiency is calculated from RCF data and averaged over 2–3 shots.

diagnostic cover different solid angles (4.51 mrad and 0.13 mrad, respectively) and spectral ranges (10s keV and up to 3.5 MeV, respectively). However, consistent trends for bremsstrahlung yields were measured with the two diagnostics. The bremsstrahlung yield measured from RCFs is significantly lower for foam targets irradiated under 45° with respect to the case of normal incidence.

3.4. Conversion efficiency

Figure 5 shows the conversion efficiency of laser energy (E_{Laser}) into bremsstrahlung photons with energy below 3.5 MeV detected by the g-cal in a solid angle of 0.13 msr (E_{BS}) for maximum laser intensity. The conversion efficiency is calculated as $\eta = E_{\mathrm{BS}}/E_{\mathrm{Laser}}$ and normalised to the value obtained with reference targets irradiated under 45° (unlike the plots in figure 2). The conversion efficiency into bremsstrahlung for flat Al targets is higher for 45° incidence than for normal incidence, with an enhancement factor of 1.6. On the contrary, the conversion efficiency for foams irradiated under normal incidence is systematically higher than that measured with any target irradiated under 45°.

The conversion efficiency of laser energy into protons can be quantified as $\eta = E_{p+}/E_{\mathrm{Laser}}$, where E_{p+} is the total proton energy detected by the specific diagnostics. For normal incidence, the conversion efficiency into protons above 4.7 MeV was evaluated using unperforated RCF stacks that cover the full proton spatial distribution. In this case, an increase by a 4.8 factor is observed for foam targets with respect to reference targets irradiated under the same conditions. For 45° incidence, conversion efficiency data based on perforated RCF stacks and TPS only allow for qualitative comparison due to the partial sampling of the proton spatial distribution, but reproduce trends very similar to those shown in figure 5 for conversion efficiency into Bremsstrahlung.

3.5. Reflected light and second harmonic

The high intensity laser pulse propagation in the foam and interaction with the solid surface was characterized for 45° incidence by imaging the light reflection off the target in specular direction onto a scatter screen (see figure 1(b)). A well-defined spot is visible in the reflected light and the second harmonic emission in the case of Al targets (figures 6(a) and (c)). On the contrary, diffused light and speckles can be observed for foam targets (figures 6(b) and (d)). The signal intensity integrated in the solid angle covered by this diagnostic is reduced by a factor 2.7 for reflected light for 4 μm foam with respect to Al targets. This reduction can be attributed to the increased absorption and larger divergence of the scattered light, that maintains a residual specularity due to reflection at the foam-substrate interface. In addition, the intensity of reflected light measured for foam targets using a band-pass filter could be decreased due to spectral broadening observed in previous studies for light propagating in a sub-critical density plasma [56].

3.6. Electron profiles and spectra

As recorded by the Lanex screen, figure 7(a) shows a clear signature of electrons accelerated from the mirror-like surface of the Al reference target along the direction of specular reflection. The spatial distribution of the signal on the Lanex screen is characterized by low signal in the area surrounding the specular reflection direction (highlighted in orange in figure 7(a)), where electrons are pushed away from the laser propagation axis by the ponderomotive potential associated to the co-propagating laser pulse. This confirms the high temporal intensity contrast of the incoming laser pulse realised by the plasma mirror

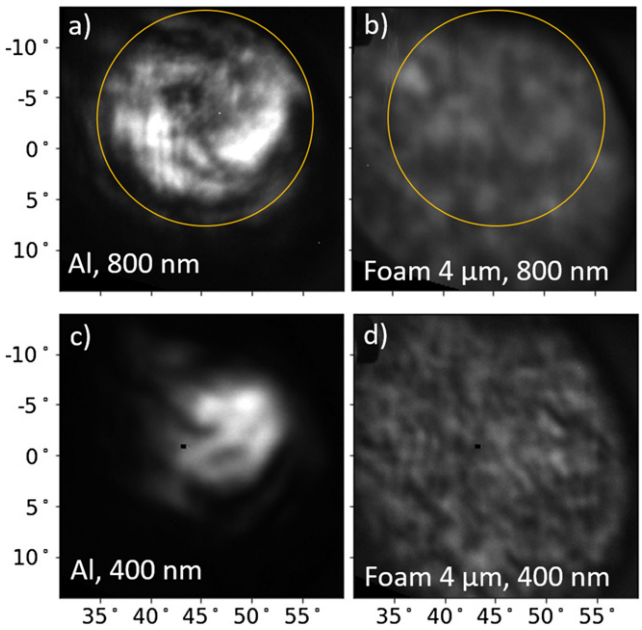

Figure 6. Images of the light pattern reflected from Al (a) and 4 μm foam (b). The orange circle indicates the expected size of the reflected beam (120 msr). Images of the second harmonic generated by Al (c) and 4 μm foam (d). Images (a)–(d) are normalized to the integrated signal intensity to allow easier comparison.

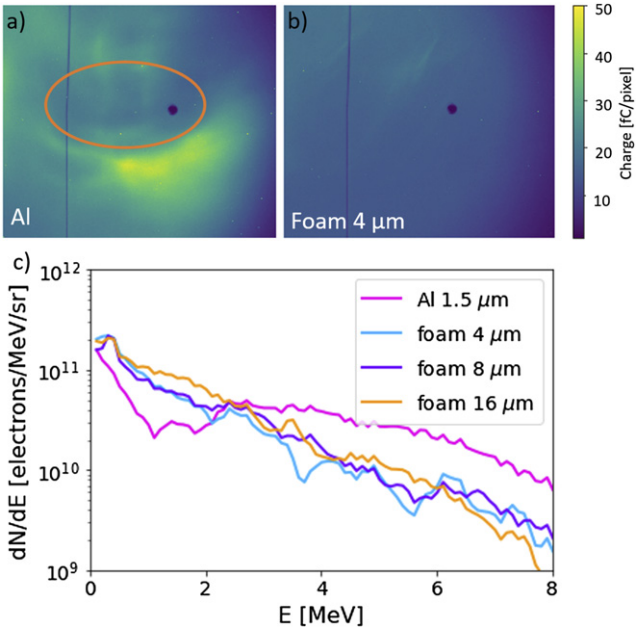

Figure 7. Images of the Lanex screen showing electrons accelerated in the direction of specular reflection from Al (a) and 4 μm foam (b). The orange oval highlights the area around the specular direction where the electron signal drops due to ponderomotive potential of the co-propagating laser pulse. (c) Representative electron spectra measured in laser propagation direction for 45° incidence angle (recorded on single shots).

[1, 57]. The integrated electron charge measured for Al targets (about 4 nC) is comparable to that observed in previous experiments with nm-thick targets [48]. This feature is not visible for foam targets (figure 7(b)).

Electron spectra were measured for 45° incidence in the laser propagation direction. Representative spectra are shown in figure 7(c). The number of detected electrons increases for all foam targets in the moderate energy range, i.e. up to 2.5 MeV, while it appears to be higher for Al foils above 2.5 MeV.

4. Discussion

Thanks to the comprehensive set of diagnostics employed in this experiment for the first time with cluster-assembled foam targets, we can examine the role of the foam structure in the interaction. Foam targets show a clear enhancement of laser energy conversion into protons and Bremsstrahlung with respect to bare Al foils for optimized experimental conditions (subsection 3.4). This is a consequence of enhanced electron generation in the inhomogeneous foam structure by the ultra-high contrast laser pulse. Survival of the foam structure until main pulse arrival is indicated by the following experimental observations. The speckles and non-specularity observed for foams from light patterns (figures 6(b) and (d)) are an indication of such feature. Moreover, strong suppression of directed electron acceleration from the target front surface in the specular direction was observed in images of the Lanex screen for foam targets with respect to Al targets (figure 7), indicating penetration of the laser within the target [1, 57]. A further signature showing that the foam structure is not significantly disrupted before the arrival of the main pulse is the non-directional acceleration of protons due to Coulomb explosion of the nanoparticles composing the foam (subsection 3.1).

Based on our experimental data and on previously published numerical results [33], it is reasonable to infer that, due to the sub-μm scale roughness of the cluster-assembled structure, the laser pulse can propagate in the foam voids and be efficiently absorbed at randomly oriented critical density surfaces around high density aggregates. The interaction with stochastic surfaces enhances the absorption due to the very high specific surface area and randomizes incident angles resulting in an increased generation of electrons driving the TNSA process. This is also consistent with the previously observed independence of the process from the light polarization [19].

Previous numerical works have highlighted differences in the interaction mechanism at play in structured and homogeneous plasmas [33]. Simulations comparing the pulse propagation in uniform and nanostructured foams show that the interaction with foams made of solid-density aggregates results in a strong increase of the absorption efficiency (for intensities between 5×10^{19} W cm^{-2} and 5×10^{20} W cm^{-2}) with respect to uniform foams, where the pulse is partially reflected due to electrons piling up at the pulse front [33]. Moreover, the nanostructure perturbs DLA [21, 33], thus reducing the maximum electron energy with respect to that theoretically achievable for electrons accelerated in a uniform near-critical plasma.

In our experiment, spectra of escaping electrons were measured for 45° incidence in the laser propagation direction (figure 7(c)), i.e. in the expected propagation direction of super-ponderomotive electrons accelerated by DLA and collimated due to magnetic confinement in the ponderomotive channel. Spectra show no evidence of superponderomotive electrons, suggesting that DLA in a ponderomotive channel typical for homogeneous foams does not occur here, as a consequence of the foam structure. The features of escaping electrons, although different with respect to Al foils, are independent of the foam thickness, as opposed to the features of the Bremsstrahlung photons and accelerated protons (figures 2–4), which are determined by the hot electrons driving the TNSA process. This confirms that the foam enhances the production of recirculating electrons that contribute to the generation of proton and photon beams.

The strong laser absorption in the foam shown by the enhanced bremsstrahlung yield for 4 μm foam with respect to bare Al (figures 4 and 5) plays an important role in explaining the dependence of the conversion efficiency on the foam thickness. It indicates that the pulse propagating in the foam is quickly depleted, so that deeper foam layers do not contribute significantly to electron generation. In fact, the monotonic decrease of the bremsstrahlung signal with the foam thickness indicates a decrease in the number of electrons reaching the substrate for thicker foams. This is also due to the broad angular distribution of the electron population, in agreement with previous numerical results [33], and the longer electron propagation path resulting in a lower transport efficiency of electrons to the substrate. Therefore electrons generated in the structured foam further away from the foam-substrate interface contribute less to the electron sheath at the target rear and the energy transferred by the laser to electrons in the foam does not necessarily contribute to the TNSA field. Yet, the broader angular distribution of the electron population also leads to a spatially extended sheath field and hence proton source size at the target rear surface, in agreement with the enhanced proton number. In addition, the pulse energy depletion and the pulse front distortion in the foam can negatively impact the generation of electrons at the foam-substrate interface, effects that become more relevant for thicker foams. Interestingly, a recent model foresees for homogeneous foams the same foam thickness scaling observed in our experiment, even though the dominating enhancement effect is due to the generation of superponderomotive electrons with a self-focused laser pulse [21].

The inferior proton and C^{6+} acceleration performance observed for 45° incidence is in part due to the longer laser and electron propagation path in the foam. However this argument does not fully explain the

difference in performances observed for normal and oblique incidence. As shown in figures 2(a) and (b), proton cut-off energies and numbers measured for 45° incidence are lower than those observed for normal incidence even for comparable effective foam thicknesses. This effect can be interpreted taking into account that electrons are generated in the foam with a broad angular distribution and that the substrate area intersecting the divergent beam is larger for 45° incidence, resulting in decreased density in the electron sheath and hence lower TNSA field at the rear target surface, especially for thick foams, falling below the field ionization threshold for C^{6+} in the case of 16 μm foam [58]. A previous study attributes the dependence on the angle of incidence to effects arising for oblique incidence, such as pulse refraction resulting in even longer pulse propagation in the foam and a mismatch in the angular distributions of electrons generated in the foam and at the foam-substrate interface, that would separate at the target rear side [21].

It is interesting to note that the monotonic dependence of proton cut-off energy and number on the foam thickness (figures 2(a) and (b)) is in agreement with previous experiments in a comparable intensity range [19, 20]. However, the proton cut-off energy and number enhancements measured in the present experiment (a factor 2 and 2.2, respectively, for TPS) are significantly higher than those measured in previous experiments (1.3 and 1.7, respectively) [19, 20]. This improvement can be ascribed to the optimization of the deposition technique enabling the production of thinner foam layers without degrading the substrate coverage, as well as to the possibility of irradiating targets under normal incidence (as opposed to 30° in previous experiments).

5. Conclusions

In conclusion, cluster-assembled foam targets have been shown to optimize conversion of laser energy into electrons relevant for TNSA, resulting in enhancement by a factor 2 and 4 in the proton cut-off energy and yield (calculated for protons with energy above 4.7 MeV), respectively, and a sixfold increase in the Bremsstrahlung yield.

As shown in figures 2, 3 and 6, the enhancement is strongly dependent on the foam thickness. Moreover, larger enhancement was observed for higher intensities (see figure 2(a)). Therefore, further proton acceleration enhancement could be expected for higher intensities, while 4 μm is presumably close to the optimal foam thickness, also considering the technical challenge to deposit thinner foams while maintaining complete surface coverage. It must however be noted that optimal foam parameters depend on the features of the incoming laser pulse, such as intensity and temporal intensity contrast.

This result is of practical interest for applications requiring high number of protons and smooth beam profile, such as ion beam analysis [44, 59] or radiobiological studies [60]. In addition, these targets provide a significant enhancement in the bremsstrahlung yield and could be optimized as pink-beam x-ray backlighters. Experimental results discussed in this paper contribute to advance the understanding of the physics of intense fs-pulses interaction with nanostructured cluster-assembled foams, thanks to an extended suite of radiation diagnostics. A comprehensive picture of the interaction mechanism will require a detailed investigation of the evolution of the foam structure to be performed using e.g. small angle x-ray scattering in pump probe experiments at XFEL facilities [61].

Acknowledgments

The work has been partially supported by EC H2020 Laserlab Europe V (PRISES), Contract No. 871124, and by the European Research Council (ERC) under the European Union's Horizon 2020 research and innovation programme (ENSURE Grant Agreement No. 647554). Support of the Institute of Ion Beam Physics and Materials Research, HZDR, is gratefully acknowledged.

Data availability statement

The data that support the findings of this study are available upon reasonable request from the authors.

ORCID iDs

Irene Prencipe https://orcid.org/0000-0003-0931-1350
Josefine Metzkes-Ng https://orcid.org/0000-0002-9556-0662

Andrea Pazzaglia https://orcid.org/0000-0001-7486-2576
David Dellasega https://orcid.org/0000-0002-7389-9307
Luca Fedeli https://orcid.org/0000-0002-7215-4178
Arianna Formenti https://orcid.org/0000-0002-7887-9313
Marco Garten https://orcid.org/0000-0001-6994-2475
Thomas Kluge https://orcid.org/0000-0003-4861-5584
Stephan Kraft https://orcid.org/0000-0002-0638-6990
Alejandro Laso Garcia https://orcid.org/0000-0002-7671-0901
Alessandro Maffini https://orcid.org/0000-0002-3388-5330
Lieselotte Obst-Huebl https://orcid.org/0000-0001-9236-8037
Martin Rehwald https://orcid.org/0000-0001-6200-6406
Karl Zeil https://orcid.org/0000-0003-3926-409X
Ulrich Schramm https://orcid.org/0000-0003-0390-7671
Thomas E. Cowan https://orcid.org/0000-0002-5845-000X
Matteo Passoni https://orcid.org/0000-0002-7844-3691

References

[1] Thévenet M, Leblanc A, Kahaly S, Vincenti H, Vernier A, Quéré F and Faure J 2016 Vacuum laser acceleration of relativistic electrons using plasma mirror injectors *Nat. Phys.* **12** 355–60
[2] Schreiber J, Bolton P R and Parodi K 2016 Invited review article: 'hands-on' laser-driven ion acceleration: a primer for laser-driven source development and potential applications *Rev. Sci. Instrum.* **87** 071101
[3] Macchi A, Borghesi M and Passoni M 2013 Ion acceleration by superintense laser-plasma interaction *Rev. Mod. Phys.* **85** 751–93
[4] Chen L M *et al* 2008 Study of x-ray emission enhancement via a high-contrast femtosecond laser interacting with a solid foil *Phys. Rev. Lett.* **100** 045004
[5] Ebert T *et al* 2020 Enhanced brightness of a laser-driven x-ray and particle source by microstructured surfaces of silicon targets *Phys. Plasmas* **27** 043106
[6] Purvis M A *et al* 2013 Relativistic plasma nanophotonics for ultrahigh energy density physics *Nat. Photon.* **7** 796–800
[7] Cerchez M *et al* 2018 Enhanced energy absorption of high intensity laser pulses by targets of modulated surface *Appl. Phys. Lett.* **112** 221103
[8] Lübcke A, Andreev A A, Höhm S, Grunwald R, Ehrentraut L and Schnürer M 2017 Prospects of target nanostructuring for laser proton acceleration *Sci. Rep.* **7** 44030
[9] Ceccotti T *et al* 2013 Evidence of resonant surface-wave excitation in the relativistic regime through measurements of proton acceleration from grating targets *Phys. Rev. Lett.* **111** 185001
[10] Margarone D *et al* 2012 Laser-driven proton acceleration enhancement by nanostructured foils *Phys. Rev. Lett.* **109** 234801
[11] Habara H, Honda S, Katayama M, Sakagami H, Nagai K and Tanaka K A 2016 Efficient energy absorption of intense ps-laser pulse into nanowire target *Phys. Plasmas* **23** 063105
[12] Jiang S *et al* 2016 Microengineering laser plasma interactions at relativistic intensities *Phys. Rev. Lett.* **116** 085002
[13] Khaghani D *et al* 2017 Enhancing laser-driven proton acceleration by using micro-pillar arrays at high drive energy *Sci. Rep.* **7** 11366
[14] Gaillard S A *et al* 2011 Increased laser-accelerated proton energies via direct laser-light-pressure acceleration of electrons in microcone targets *Phys. Plasmas* **18** 056710
[15] Kluge T *et al* 2012 High proton energies from cone targets: electron acceleration mechanisms *New J. Phys.* **14** 023038
[16] Bin J H *et al* 2015 Ion acceleration using relativistic pulse shaping in near-critical-density plasmas *Phys. Rev. Lett.* **115** 064801
[17] Bin J H 2018 Enhanced laser-driven ion acceleration by superponderomotive electrons generated from near-critical-density plasma *Phys. Rev. Lett.* **120** 074801
[18] Ma W J *et al* 2019 Laser acceleration of highly energetic carbon ions using a double-layer target composed of slightly underdense plasma and ultrathin foil *Phys. Rev. Lett.* **122** 014803
[19] Passoni M *et al* 2016 Toward high-energy laser-driven ion beams: nanostructured double-layer targets *Phys. Rev. Accel. Beams* **19** 061301
[20] Prencipe I *et al* 2016 Development of foam-based layered targets for laser-driven ion beam production *Plasma Phys. Control. Fusion* **58** 034019
[21] Pazzaglia A, Fedeli L, Formenti A, Maffini A and Passoni M 2020 A theoretical model of laser-driven ion acceleration from near-critical double-layer targets *Commun. Phys.* **3** 133
[22] Wang H Y *et al* 2011 Laser shaping of a relativistic intense, short Gaussian pulse by a plasma lens *Phys. Rev. Lett.* **107** 265002
[23] Mourou G A, Tajima T and Bulanov S V 2006 Optics in the relativistic regime *Rev. Mod. Phys.* **78** 309–71
[24] Palaniyappan S *et al* 2012 Dynamics of relativistic transparency and optical shuttering in expanding overdense plasmas *Nat. Phys.* **8** 763–9
[25] Cattani F, Kim A, Anderson D and Lisak M 2000 Threshold of induced transparency in the relativistic interaction of an electromagnetic wave with overdense plasmas *Phys. Rev.* E **62** 1234–7
[26] Robinson A P L, Trines R M G M, Dover N P and Najmudin Z 2012 Hole-boring radiation pressure acceleration as a basis for producing high-energy proton bunches *Plasma Phys. Control. Fusion* **54** 115001
[27] Nagai K, Musgrave C S A and Nazarov W 2018 A review of low density porous materials used in laser plasma experiments *Phys. Plasmas* **25** 030501
[28] Pukhov A and Meyer-Ter-Vehn J 1996 Relativistic magnetic self-channeling of light in near-critical plasma: three-dimensional particle-in-cell simulation *Phys. Rev. Lett.* **76** 3975–8
[29] Borghesi M, MacKinnon A J, Barringer L, Gaillard R, Gizzi L A, Meyer C, Willi O, Pukhov A and Meyer-ter-Vehn J 1997 Relativistic channeling of a picosecond laser pulse in a near-critical preformed plasma *Phys. Rev. Lett.* **78** 879–82

[30] Gahn C, Tsakiris G D, Pukhov A, Meyer-ter-Vehn J, Pretzler G, Thirolf P, Habs D and Witte K J 1999 Multi-MeV electron beam generation by direct laser acceleration in high-density plasma channels *Phys. Rev. Lett.* **83** 4772–5
[31] Pukhov A, Sheng Z M and Meyer-ter-Vehn J 1999 Particle acceleration in relativistic laser channels *Phys. Plasmas* **6** 2847–54
[32] Arber T D *et al* 2015 Contemporary particle-in-cell approach to laser-plasma modelling *Plasma Phys. Control. Fusion* **57** 113001
[33] Fedeli L, Formenti A, Cialfi L, Pazzaglia A and Passoni M 2018 Ultra-intense laser interaction with nanostructured near-critical plasmas *Sci. Rep.* **8** 3834
[34] Fedeli L, Formenti A, Pazzaglia A, Arioli F M, Tentori A and Passoni M 2020 Enhanced laser-driven hadron sources with nanostructured double-layer targets *New J. Phys.* **22** 033045
[35] Jiang K, Pukhov A and Zhou C T 2020 TJ cm^{-3} high energy density plasma formation from intense laser-irradiated foam targets composed of disordered carbon nanowires *Plasma Phys. Control. Fusion* **63** 015014
[36] Passoni M *et al* 2014 Energetic ions at moderate laser intensities using foam-based multi-layered targets *Plasma Phys. Control. Fusion* **56** 045001
[37] Zeil K *et al* 2010 The scaling of proton energies in ultrashort pulse laser plasma acceleration *New J. Phys.* **12** 045015
[38] Obst L *et al* 2018 On-shot characterization of single plasma mirror temporal contrast improvement *Plasma Phys. Control. Fusion* **60** 054007
[39] Schramm U *et al* 2017 First results with the novel petawatt laser acceleration facility in Dresden *J. Phys.: Conf. Ser.* **874** 012028
[40] Zani A, Dellasega D, Russo V and Passoni M 2013 Ultra-low density carbon foams produced by pulsed laser deposition *Carbon* **56** 358–65
[41] Prencipe I, Dellasega D, Zani A, Rizzo D and Passoni M 2015 Energy dispersive x-ray spectroscopy for nanostructured thin film density evaluation *Sci. Technol. Adv. Mater.* **16** 025007
[42] Pazzaglia A, Maffini A, Dellasega D, Lamperti A and Passoni M 2019 Reference-free evaluation of thin films mass thickness and composition through energy dispersive x-ray spectroscopy *Mater. Charact.* **153** 92–102
[43] Maffini A, Pazzaglia A, Dellasega D, Russo V and Passoni M 2019 Growth dynamics of pulsed laser deposited nanofoams *Phys. Rev. Mater.* **3** 083404
[44] Passoni M *et al* 2020 Advanced laser-driven ion sources and their applications in materials and nuclear science *Plasma Phys. Control. Fusion* **62** 014022
[45] Chen C D *et al* 2008 A bremsstrahlung spectrometer using *k*-edge and differential filters with image plate dosimeters *Rev. Sci. Instrum.* **79** 10E305
[46] Hannasch A *et al* 2021 Compact spectroscopy of keV to MeV x-rays from a laser wakefield accelerator *Sci. Rep.* **11** 14368
[47] Kurz T *et al* 2018 Calibration and cross-laboratory implementation of scintillating screens for electron bunch charge determination *Rev. Sci. Instrum.* **89** 093303
[48] Poole P L L *et al* 2018 Laser-driven ion acceleration via target normal sheath acceleration in the relativistic transparency regime *New J. Phys.* **20** 013019
[49] Roth M *et al* 2002 Energetic ions generated by laser pulses: a detailed study on target properties *Phys. Rev. Spec. Top. Accel. Beams* **5** 061301
[50] Fuchs J *et al* 2003 Spatial uniformity of laser-accelerated ultrahigh-current mev electron propagation in metals and insulators *Phys. Rev. Lett.* **91** 255002
[51] Manclossi M, Santos J J, Batani D, Faure J, Debayle A, Tikhonchuk V T and Malka V 2006 Study of ultraintense laser-produced fast-electron propagation and filamentation in insulator and metal foil targets by optical emission diagnostics *Phys. Rev. Lett.* **96** 125002
[52] Metzkes J, Kluge T, Zeil K, Bussmann M, Kraft S D, Cowan T E and Schramm U 2014 Experimental observation of transverse modulations in laser-driven proton beams *New J. Phys.* **16** 023008
[53] Margarone D *et al* 2015 Laser-driven high-energy proton beam with homogeneous spatial profile from a nanosphere target *Phys. Rev. Spec. Top. Accel. Beams* **18** 071304
[54] Fedeli L, Formenti A, Cialfi L, Sgattoni A, Cantono G and Passoni M 2018 Structured targets for advanced laser-driven sources *Plasma Phys. Control. Fusion* **60** 014013
[55] D'Agostini G 2010 Improved iterative Bayesian unfolding (arXiv:1010.0632)
[56] Levy D *et al* 2020 Laser-plasma proton acceleration with a combined gas-foil target *New J. Phys.* **22** 103068
[57] Chopineau L *et al* 2019 Identification of coupling mechanisms between ultraintense laser light and dense plasmas *Phys. Rev.* X **9** 011050
[58] Hegelich M *et al* 2002 MeV ion jets from short-pulse-laser interaction with thin foils *Phys. Rev. Lett.* **89** 085002
[59] Passoni M, Fedeli L and Mirani F 2019 Superintense laser-driven ion beam analysis *Sci. Rep.* **9** 9202
[60] Brack F-E *et al* 2020 Spectral and spatial shaping of laser-driven proton beams using a pulsed high-field magnet beamline *Sci. Rep.* **10** 9118
[61] Kluge T, Gutt C, Huang L G, Metzkes J, Schramm U, Bussmann M and Cowan T E 2014 Using x-ray free-electron lasers for probing of complex interaction dynamics of ultra-intense lasers with solid matter *Phys. Plasmas* **21** 033110